

Configurational entropy and spectroscopy of pomeron resonances in dynamical AdS/QCD

D. Marinho Rodrigues^{1,2,*} and R. da Rocha^{1,†}

¹*Federal University of ABC, Center of Mathematics, Santo André, 09580-210, Brazil*

²*Federal University of ABC, Center of Physics, Santo André, 09580-210, Brazil*

Pomeron resonances in AdS/QCD are here studied using the configurational entropy (CE). The concept of CE Regge trajectories, associating the CE of the pomeron resonances with both their spin J^{PC} and to their mass spectra, is used to derive the mass spectra of higher J^{PC} pomeron resonances. For it, the linear, the exponential modified and the anomalous quadratic dilatonic models, each one with linear and logarithmic anomalous corrections, are employed. Several methods are implemented, hybridizing AdS/QCD and established data of lattice QCD.

PACS numbers: 89.70.Cf, 11.25.Tq, 12.39.Mk

I. INTRODUCTION

The configurational entropy (CE) displays the compression rate of all information flowing through a system, in the limit where no losses are regarded. Information is compressed into momentum space modes, that comprise a given physical system, as firstly proposed by Shannon [1]. In this sense, the CE constitutes a bound on the transmission rate of information sources. The CE can probe and also measure the information that composes the correlations among these modes, thus converting into a coded form the complexity of shape in the studied system [2, 3]. Localized solutions of PDEs are examples of non-trivial spatial complexity, as well as the correlation of thermal fluctuations in systems that go through phase transitions. For computing the CE, a spatially-localized integrable scalar field is necessary. The energy density, taken as the time component of the energy-momentum tensor, is a prime scalar field candidate [4]. However, other localized scalar fields, like the nuclear cross-section and scattering amplitudes have been used in different QCD contexts [5–8]. The CE has been demonstrated to consist of a very useful apparatus to study and predict the prevalence, abundance, and dominance of physical states and their resonances. The recently obtained results, in the literature, mainly in QCD and AdS/QCD setups, match and corroborate to phenomenological data in PDG [9], as well as provide relevant predictions for future experiments, mainly in LHC.

The CE has been playing important roles in scrutinizing AdS/QCD (both hardwall and softwall) models, studying relevant properties in QCD, and its phenomenology. Several new methods and procedures, also involving the existence of CE Regge trajectories, have been employed to investigate diverse families of light-flavor mesonic states and excitations, in chiral-gluon condensates and dilaton-graviton backgrounds [10–12], also

including tachyonic ones [13]. Besides, tensor mesons [14] and scalar glueballs [15] were explored under CE tools. Quarkonia states, both at zero temperature [16] and at finite temperature [17], were investigated, with relevant physical features regarding phenomenology and the configurational stability of bottomonium and charmonium resonances. Besides, quarkonia and plasmas with finite density were studied, from the CE point of view, in Ref. [18]. Refs. [5–8, 19] studied gluons and quarks in the color glass condensate regime of QCD, exhibiting new features and applications of CE, and providing a theoretical explanation for diverse parameters, previously used in the literature to best fit experimental data. In the cold quark-gluon plasma, Korteweg-de Vries solitons, consisting of localized pulses, were also analyzed via the CE. These pulses, propagating almost without any shape distortion, are governed by a relevant parameter to describe the system at its most compressed state, whose choices match phenomenological data [20]. More on the use of CE in QCD was studied in Ref. [21]. Standard and exotic baryonic excitations were scrutinized in Ref. [22], also in a finite temperature setup [23]. The configurational stability of boson stars and black holes were also explored, using the CE, in Refs. [24–29]. Also, phase transitions [30], topological defects [31–34] and aspects of particle physics [35, 36] were discussed with the use of the CE. The quantum version of the classical Shannon entropy is detailedly exposed in Ref. [37].

The AdS/QCD setup has been proved to be an important tool to investigate non-perturbative aspects of QCD, as, for example, confinement [38–43]. The hard and the softwall models represent thriving approaches of AdS/QCD that match data in PDG [44–46]. In the gauge/gravity duality dictionary, fields in the AdS₅ bulk represent dual quantities to operators of QCD on the boundary.

Several phenomenological approaches to scrutinize non-perturbative features of QCD consist in probing particle states, and their resonances. QCD predicts gluonic bound states, comprising glueballs, to exist. Therefore the quest for the glueball content of hadrons plays an important role. One of these approaches is based on the

*Electronic address: diegomr@if.ufrj.br

†Electronic address: roldao.rocha@ufabc.edu.br

construction of phenomenological Lagrangians capable of taking into account gluonic processes in hadronic interactions [47]. Lattice QCD computations derived the glueball spectrum in many setups [48, 49]. Previous approaches proposed the QCD vacuum structure to be fulfilled with a condensate of scalar glueballs [50]. When one employs solutions of the equations of motion for massive gluons, glueball masses can be derived, in full compliance with QCD lattice phenomenology. Then, the complex pomeron trajectory can be obtained, whose real projection regards the soft pomeron, with support of HERA data [48]. Among prominent topics in the physics of hadrons, the relationship between pomerons and glueballs plays a prominent role [51]. The pomeron itself represents the well-known Pomernanchuk trajectory. It can be seen as the vacuum exchange to high energetic scattering phenomena, occurring when $\frac{1}{N_c}$ leading terms set in. QCD poses the pomeron as the exchange of two gluons, leastwise, in any color singlet state in QFT [49].

Our main aim here is to use techniques of CE, already well succeeded in QCD applications, to study pomeron resonances, also in the context of AdS/QCD. Configurational-entropic Regge trajectories are the main tool to derive the mass spectra of higher spin pomeron resonances, in different dilaton models. Both AdS/QCD and lattice QCD data are going to be used, for it.

This paper is organized as follows: Sect. II briefly reviews the holographic setup used in this work, namely, the background geometry and glueball spectra. Sect. III discusses the results concerning the CE applied to pomeron resonances, including a comprehensive analysis of the CE Regge trajectories and the derivation of the mass spectra of pomeron family resonances, in six dilaton models. The conclusions and more discussion are comprised of Sect. IV.

II. HOLOGRAPHIC SETUP

Here the holographic model in Refs. [52, 53], based on the dynamical softwall model, will be used. Next, the results for the quadratic dilaton profile are reviewed. Then, this holographic model is applied to the linear and exponential dilaton profiles.

The dynamical softwall model is characterized by an Einstein-dilaton action, in the Einstein frame, given by

$$S = \frac{1}{16\pi G_5} \int d^5x \sqrt{-g} \left(R - \frac{4}{3} g^{\mu\nu} \partial_\mu \phi \partial_\nu \phi + V(\phi) \right), \quad (1)$$

where G_5 is the 5-dimensional Newton's constant, $g = \det(g_{\mu\nu})$, R denotes the Ricci scalar, ϕ is the dilaton field and $V(\phi)$ stands for the dilaton potential. The equations of motion, derived from the action (1), are given by

$$E_{\mu\nu} - \frac{4}{3} \left(\partial_\mu \phi \partial_\nu \phi - \frac{1}{2} g_{\mu\nu} (\partial\phi)^2 \right) - \frac{1}{2} g_{\mu\nu} V(\phi) = 0, \quad (2)$$

$$g^{\mu\nu} \partial_\mu \partial_\nu \phi + \frac{3}{8} \frac{\partial V(\phi)}{\partial \phi} = 0, \quad (3)$$

with the Einstein tensor $E_{\mu\nu}$ defined as

$$E_{\mu\nu} = R_{\mu\nu} - \frac{1}{2} g_{\mu\nu} R. \quad (4)$$

In order to solve the equations of motion, the metric ansatz to be considered here is given by¹ [54]

$$ds^2 = \frac{1}{\zeta(z)^2} (dz^2 - dt^2 + d\vec{x}^2), \quad (5)$$

$$\phi = \phi(z). \quad (6)$$

Plugging this ansatz in Eqs. (2, 3) yields

$$\frac{\zeta''(z)}{\zeta(z)} = \frac{4}{9} \phi'(z)^2, \quad (7)$$

$$V(\phi) = 12 \zeta'(z)^2 - \frac{4}{3} \zeta(z)^2 \phi'(z)^2. \quad (8)$$

The advantage of this dynamical AdS/QCD model is that the background is a consistent solution of Einstein's equations and, within it, one can implement confinement, characterized by an area-law for the Wilson loop, and linear Regge trajectories (see for instance [55]).

A. Quadratic Dilaton Profile

Considering the quadratic dilaton profile $\phi(z) = \pm k z^2$, the solution for $\zeta(z)$, and the dilaton potential, read

$$\zeta(z) = z {}_0F_1 \left(\frac{5}{4}; \frac{k^2 z^4}{4} \right), \quad (9)$$

$$V(\phi) = 12 {}_0F_1 \left(\frac{1}{4}; \frac{\phi^2}{9} \right)^2 - \frac{16}{3} \phi^2 {}_0F_1 \left(\frac{5}{4}; \frac{\phi^2}{9} \right)^2, \quad (10)$$

where ${}_0F_1(a; z)$ denotes the confluent hypergeometric function. The integration constants were chosen so that $\zeta(z) \rightarrow z$ in the UV regime ($z \rightarrow 0$). Besides, the solution for $\zeta(z)$ can be still put into the Bessel form, given by

$$\zeta(z) = \left(\frac{3}{k} \right)^{1/4} \Gamma \left(\frac{5}{4} \right) \sqrt{z} I_{\frac{1}{4}} \left(\frac{2}{3} k z^2 \right), \quad (11)$$

where $I_\nu(z)$ is the modified Bessel function of first kind.

The UV expansions for $\zeta(z)$ and $V(\phi)$ read

$$\zeta(z) = z + \frac{4}{45} k^2 z^5 + \mathcal{O}(z^6), \quad (12)$$

$$V(\phi) = 12 + \frac{16}{3} \phi^2 + \mathcal{O}(\phi^4). \quad (13)$$

Therefore, one can see that, near the UV, the geometry is asymptotically AdS.

¹ In this work the AdS radius L is set to unity.

On the other hand, the IR expansions, i.e., $z \rightarrow \infty$, go like

$$\zeta(z) \simeq e^{\frac{2}{3}kz^2} \quad (14)$$

$$V(\phi) \simeq e^{\frac{4}{3}\phi}. \quad (15)$$

Here, it is worth to point out that, although the full solutions for $\zeta(z)$ and $V(\phi)$, respectively in Eqs. (9) and (10), are independent of the sign of the dilaton profile, to get the proper IR behavior one should stick to the positive sign for the dilaton field. Otherwise one would violate the confinement criteria, established in Refs. [56, 57].

B. Linear Dilaton Profile

Now, considering the linear dilaton profile, $\phi(z) = \sqrt{k}z$, the solutions for $\zeta(z)$ and the dilaton potential respectively read

$$\zeta(z) = \frac{3 \sinh\left(\frac{2\sqrt{k}z}{3}\right)}{2\sqrt{k}}, \quad (16)$$

$$V(\phi) = \frac{3}{2} \left[5 + 3 \cosh\left(\frac{4\phi}{3}\right) \right]. \quad (17)$$

The UV expansions, for $\zeta(z)$ and $V(\phi)$, in this case take the form

$$\zeta(z) = z + \frac{2}{27}kz^3 + \mathcal{O}(z^5), \quad (18)$$

$$V(\phi) = 12 + 4\phi^2 + \mathcal{O}(\phi^4). \quad (19)$$

Again, the UV regime yields the geometry to be asymptotically AdS.

Besides, the IR expansions yield

$$\zeta(z) \simeq e^{\frac{2}{3}\sqrt{k}z} \quad (20)$$

$$V(\phi) \simeq e^{\frac{4}{3}\phi}, \quad (21)$$

which looks very similar to the IR expansion for the quadratic dilaton case.

C. Exponential Dilaton Profile

Here, the background described by the action (1) is investigated, with a modified exponential dilaton profile, given by [59]

$$\phi(z) = kz^2(1 - e^{-kz^2}), \quad (22)$$

whose asymptotic behavior interpolates between the quadratic dilaton profile, $\phi(z) = kz^2$, in the IR regime, and a quartic dilaton profile, $\phi(z) = kz^4$, in the UV limit. This profile was used in Ref. [59], in the context of the meson spectra and chiral phase transitions, providing quite good results. Here we want to study the effect

of this profile from the point of view of the even-spin glueball spectra, associated with the pomeron, using the CE.

In Fig. 1 the exponential dilaton profile is shown, for several values of k in GeV^2 .

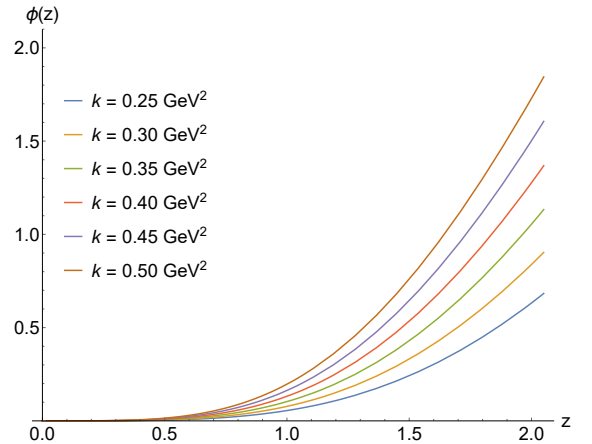


FIG. 1: Exponential dilaton $\phi(z)$ (22) profile, for several values of k in GeV^2 .

By using a shooting method, one can numerically solve Eqs. (7, 8), integrating from the UV boundary towards the IR one. The boundary condition $\zeta(z) \rightarrow z$ was used in the UV, i.e., one imposes the background asymptotically approaches AdS, in the UV. The numerical solution for the warp factor $\zeta(z)$ is displayed in Fig. 2, for several values of k , including $k = 0$, where one recovers the pure AdS case, i.e., $\zeta(z) \rightarrow z$.

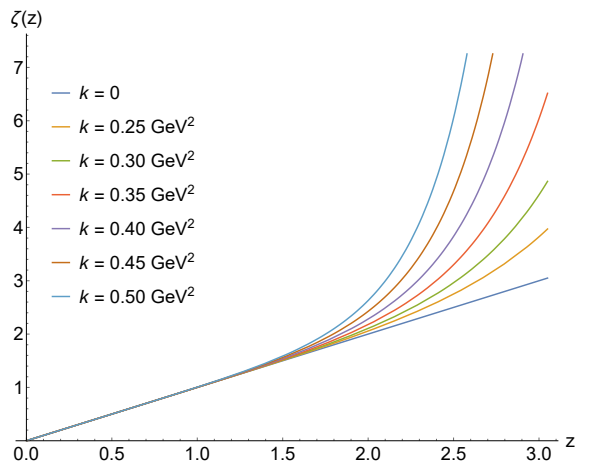


FIG. 2: Warp factor $\zeta(z)$, for several values of k in GeV^2 .

In Figs. 3 and 4, respectively, the dilaton potential $V(\phi)$, given by (8), and its first derivative as a function of ϕ , are respectively displayed, for several values of k .

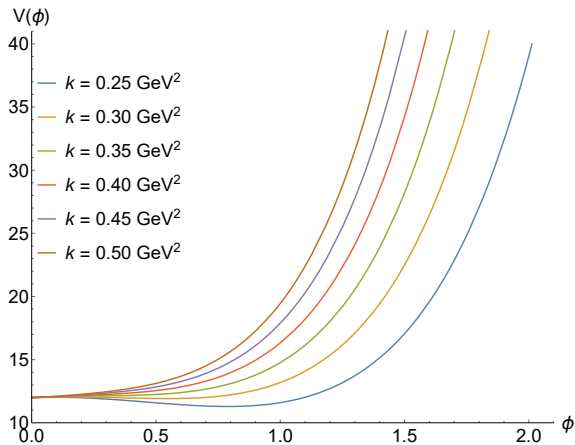


FIG. 3: Dilaton potential $V(\phi)$ for several values of k in GeV^2 .

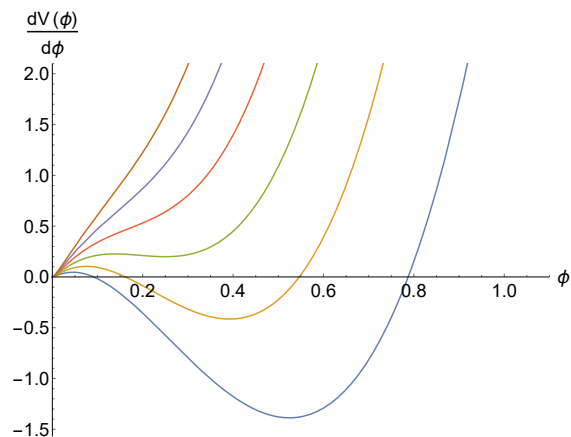


FIG. 4: First derivative of the dilaton potential $V(\phi)$ for several values of k in GeV^2 . The color legends for each value of k in this case are the same as in Fig. 3.

One can see that there are some values of k for which the potential is non-monotonic. As discussed in Ref. [58], here we will take a value of k for which the potential is a monotonically increasing function, to prevent the appearance of conformal fixed points, making sure that the AdS is the true vacuum solution for $\phi = 0$. For this reason we anticipate that $k = 0.35 \text{ GeV}^2$ will be fixed, for the exponential dilaton profile in Eq. (22). No larger value for k could be chosen, otherwise the mass of the scalar glueball and higher-spin resonances would be too high, in comparison with the literature.

D. Glueball Action and Mass Spectra

The glueball action, in the string frame, reads [52]

$$S = \int d^5x \sqrt{-g} e^{-\phi(z)} [g^{MN} \partial_M \mathcal{G} \partial_N \mathcal{G} + M_5^2 \mathcal{G}^2], \quad (23)$$

where M_5 is the mass of the scalar field $\mathcal{G}(x)$ in 5 dimensions. The relation between string frame quantities

and Einstein frame ones, already obtained in the previous subsections, is the following

$$\zeta_s(z) = \zeta(z) e^{-\frac{2}{3} \phi(z)}, \quad (24)$$

$$V_s(\phi) = V(\phi) e^{-\frac{4}{3} \phi(z)}, \quad (25)$$

where the subscript “s” denotes a quantity in the string frame, whereas $\zeta(z)$ and $V(\phi)$, respectively given by (9) and (10), are in the Einstein frame, for the quadratic dilaton case, and (16) and (17) for the linear dilaton case.

The equations of motion from (23) read

$$\partial_M [\sqrt{-g_s} e^{-\phi(z)} g^{MN} \partial_N \mathcal{G}] - \sqrt{-g_s} e^{-\phi(z)} M_5^2 \mathcal{G} = 0. \quad (26)$$

Using the ansatz

$$\mathcal{G}(x^\mu, z) = e^{i q^\mu x_\mu + \frac{B(z)}{2}} \psi(z), \quad B(z) = \phi + 3 \ln \zeta_s(z), \quad (27)$$

one obtains a Schrödinger-like equation given by

$$-\psi'' + V_{\text{Sch}}(z) \psi = (-q^2) \psi, \quad (28)$$

where $-q^2 = m_n^2$, where m_n are the glueball masses, $n = 0, 1, \dots$ denotes the radial excitations, and V_{Sch} is the Schrödinger potential given by

$$V_{\text{Sch}}(z) = \left(\frac{B'^2}{4} - \frac{B''}{2} + M_5^2 \zeta^{-2} e^{\frac{4}{3} \phi(z)} \right), \quad (29)$$

where the relation (24) between ζ_s and $\zeta(z)$ was used.

For higher spin fields in AdS, the following mass relation will be considered [60]

$$M_5^2 = J(J+4) - J + \gamma(J), \quad (30)$$

where one already considers twist-4 ($\Delta - J = 4$) even-spin glueball operators $\mathcal{O}_{4+J} \equiv J^{PC}$, with $P = C = +1$, where P is the parity and C the charge conjugation. Besides, a contribution coming from the anomalous dimension $\gamma(J)$ is also included, for the glueball operator.

Concerning the anomalous dimensions, we are going to consider it depending on the spin J in two different forms, which we will call by *anomalous I* and *anomalous II*, respectively given by:

$$\gamma^I(J) = \gamma_0 J \quad (\text{anomalous I}) \quad (31)$$

$$\gamma^{II}(J) = \gamma_0 \ln(1+J) \quad (\text{anomalous II}) \quad (32)$$

so that for $J = 0$, $\gamma^{II}(J)$ reduces to $\gamma^I(J)$.

1. Quadratic Dilaton

For the quadratic dilaton profile, Eq. (28) was solved numerically in [52, 61, 62] in different contexts. In Ref. [53], Eq. (28) was analytically solved, giving glueball masses in good agreement with QCD lattice data.

The mass spectra of the pomeron family, for both the lattice QCD and the dynamical AdS/QCD model, and taking into account both the anomalous dimensions I and

II, given by (31) and (32), respectively, are displayed in Tables I and II. The values of k and γ_0 were chosen to better fit low J^{PC} pomeron resonances with lattice QCD data (for more details see [53] and references therein).

J^{PC}	Mass [AdS/QCD]	Mass [lattice QCD]	Mass [Ref. [63]]
0	1.84	1.595	
2	2.64	2.39	1.758
4	3.52	3.80	3.198
6	4.42	4.48	4.249
8	5.31		5.165
10	6.21		
12	7.10		
14	7.99		
16	8.88		
18	9.77		

TABLE I: Mass spectra (GeV) of even-spin glueballs as a function of J^{PC} , in the dynamical AdS/QCD model using the anomalous dimension I (31) (second column), in the lattice QCD (third column), and in DP Regge model [63] (fourth column).

The results presented in Table I were taken from Ref. [53], for the anomalous I case. For the anomalous II case, we have just used the analytically mass spectra obtained therein and computed the glueball masses, substituting the anomalous dimension I by II, given by (32).

J^{PC}	Mass [AdS/QCD]	Mass [lattice QCD]	Mass [Ref.[63]]
0	0.82	1.595	
2	2.11	2.39	1.758
4	3.21	3.80	3.198
6	4.25	4.48	4.249
8	5.26		5.165
10	6.27		
12	7.64		
14	8.64		
16	9.63		
18	10.6		

TABLE II: Mass spectra (GeV) of even-spin glueballs as a function of J^{PC} , in the dynamical AdS/QCD model using the anomalous dimension II (32) (second column), in the lattice QCD (third column), and in DP Regge model [63] (fourth column).

As an example, with the data in the second column of Table I one can reproduce the Regge trajectory of the pomeron family, illustrated by Fig. 5 in the dynamical AdS/QCD model. Besides, using data in the third

column of Table I, the Regge trajectory of the pomeron family, is depicted in Fig. 5 in lattice QCD.

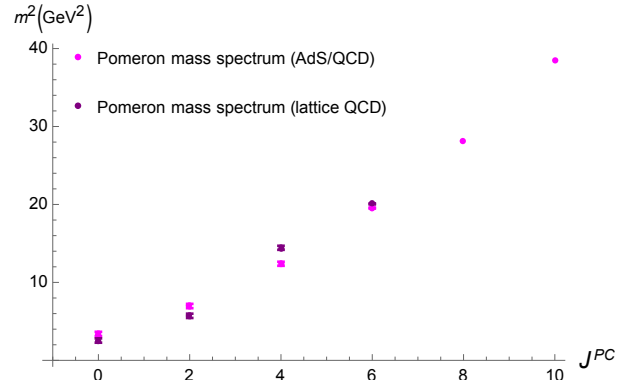


FIG. 5: (Squared) mass spectra of even-spin glueballs as a function of J^{PC} , in both in lattice QCD (purple points), containing just even-spin glueballs, for $J^{PC} = 0, 2, 4, 6$; and in the AdS/QCD model (magenta points), for $J^{PC} = 0, 2, \dots, 10$, with the respective error bars.

2. Linear Dilaton

Now, we turn to the linear dilaton profile. Despite the fact that the linear dilaton is simpler, compared to the quadratic one, we could not find any analytical solution for Eq. (28), as obtained in [53]. In this way, we had to solve it numerically, through the *NDEingensystem* routine in *Mathematica*, to obtain the mass spectra from (28). The best fit parameters were found to be

$$(\sqrt{k}, \gamma_0) = (0.505 \text{ GeV}, -1.995), \quad \text{anomalous I,} \quad (33)$$

$$(\sqrt{k}, \gamma_0) = (0.445 \text{ GeV}, -1.5), \quad \text{anomalous II.} \quad (34)$$

The results, for the obtained mass spectra, are displayed in Tables III and IV, for both the anomalous I and anomalous II cases, respectively.

J^{PC}	Mass [AdS/QCD]	Mass [lattice QCD]	Mass [Ref. [63]]
0	0.88	1.595	
2	1.90	2.39	1.758
4	3.18	3.80	3.198
6	4.50	4.48	4.249
8	5.83		5.165
10	7.17		
12	8.51		
14	9.86		
16	11.2		
18	12.5		

TABLE III: Mass spectra (GeV) of even-spin glueballs as a function of J^{PC} , in the dynamical AdS/QCD model using the anomalous dimension I (31) (second column), in the lattice QCD (third column), and in DP Regge model [63] (fourth column).

J^{PC}	Mass [AdS/QCD]	Mass [lattice QCD]	Mass [Ref. [63]]
0	0.82	1.595	
2	1.95	2.39	1.758
4	3.18	3.80	3.198
6	4.40	4.48	4.249
8	5.62		5.165
10	6.83		
12	8.04		
14	9.25		
16	10.4		
18	11.6		

TABLE IV: Mass spectra (GeV) of even-spin glueballs as a function of J^{PC} , in the dynamical AdS/QCD model using the anomalous dimension II (32) (second column), in the lattice QCD (third column), and in DP Regge model [63] (fourth column).

3. Exponential Dilaton

For the exponential dilaton profile (22), we also had to solve numerically Eq. (28), to obtain the mass spectra. The best fit parameters read

$$(k, \gamma_0) = (0.35 \text{ GeV}^2, -5), \quad \text{anomalous I,} \quad (35)$$

$$(k, \gamma_0) = (0.35 \text{ GeV}^2, -9.1), \quad \text{anomalous II.} \quad (36)$$

The results for the mass spectra obtained are displayed in Tables V and VI for both the anomalous I and II cases, respectively.

J^{PC}	Mass [AdS/QCD]	Mass [lattice QCD]	Mass [Ref. [63]]
0	2.05	1.595	
2	2.05	2.39	1.758
4	3.37	3.80	3.198
6	5.00	4.48	4.249
8	6.69		5.165
10	8.40		
12	8.80		
14	9.08		
16	9.32		
18	9.51		

TABLE V: Mass spectra (GeV) of even-spin glueballs as a function of J^{PC} , in the dynamical AdS/QCD model using the anomalous dimension II (32) (second column), in the lattice QCD (third column), and in DP Regge model [63] (fourth column).

J^{PC}	Mass [AdS/QCD]	Mass [lattice QCD]	Mass [Ref. [63]]
0	2.05	1.595	
2	2.05	2.39	1.758
4	4.00	3.80	3.198
6	5.93	4.48	4.249
8	7.80		5.165
10	8.71		
12	9.03		
14	9.28		
16	9.49		
18	9.67		

TABLE VI: Mass spectra (GeV) of even-spin glueballs as a function of J^{PC} , in the dynamical AdS/QCD model using the anomalous dimension II (32) (second column), in the lattice QCD (third column), and in DP Regge model [63] (fourth column).

Interestingly, for the exponential dilaton, in both cases (anomalous I and II) the best fit parameters (k and γ_0) provided a mass spectrum with degenerate scalar and tensorial glueballs, i.e.,

$$\frac{m_{2^{++}}}{m_{0^{++}}} = 1. \quad (37)$$

Similar findings were first observed in Ref. [64], and then in [60, 65], in the context of twist-2 operators, wherein the transversal and traceless part of the spin-2 field $h_{\mu\nu}$ satisfy the same field equation as the scalar field, explaining this degeneracy.

Finally, for the sake of completeness Figs. 6 and 7 show the Schrödinger potentials (29), for several values

of spin J up to $J = 10$, for both the anomalous I and II cases, respectively.

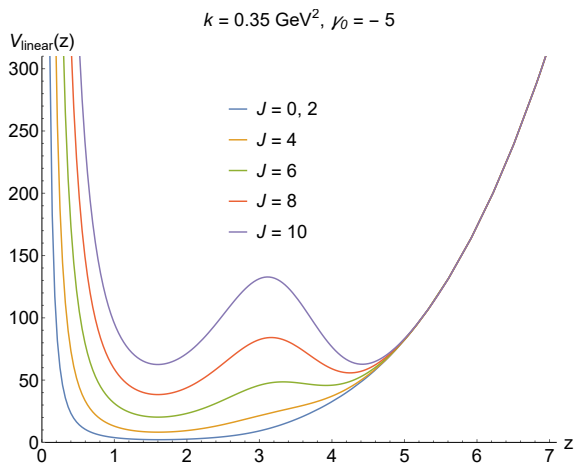


FIG. 6: Schrödinger potential (29) for the anomalous I case, V_{linear} , for several values of spin J , up to $J = 10$.

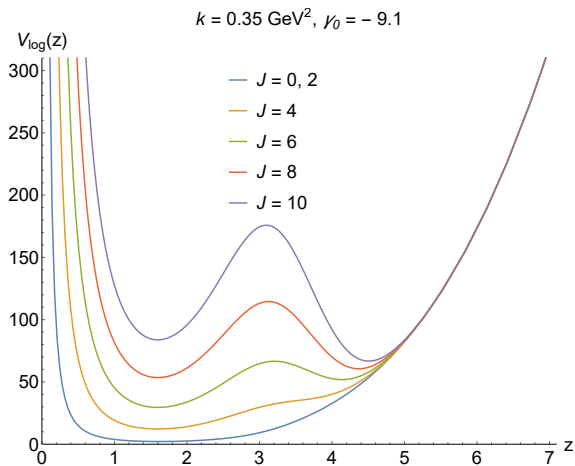


FIG. 7: Schrödinger potential (29) for the anomalous II case, V_{log} , for several values of spin J , up to $J = 10$.

III. CE REGGE TRAJECTORIES OF POMERON RESONANCES AND MASS SPECTRA

The fundamental concept underlying the CE regards a measure of the correlations among scalar field fluctuations that describe the physical system to be studied. To portray the system, the energy density – the time component of the stress-energy-momentum tensor $T_{00}(\vec{r}) = \rho(\vec{r})$ – is the essential ingredient, where $\vec{r} \in \mathbb{R}^n$. The well-known 2-point function $\Upsilon(\vec{r}) = \int \cdots \int_{\mathbb{R}^n} \rho(\vec{v} + \vec{r})\rho(\vec{v}) d\vec{v}$ defines a probability distribution [17] that makes the CE to be precisely the (Shannon) information entropy of correlations.

For computing the CE, one first calculates the Fourier transform

$$\rho(\vec{k}) = \frac{1}{(2\pi)^{n/2}} \int \cdots \int_{\mathbb{R}^n} \rho(\vec{r}) e^{-i\vec{k}\cdot\vec{r}} d^n x, \quad (38)$$

whose squared norm is the power spectrum. With it in hands, another important quantity, representing the correlation probability distribution in the momentum space, is defined by the so-called modal fraction, as [3]

$$\rho(\vec{k}) = \frac{|\rho(\vec{k})|^2}{\int \cdots \int_{\mathbb{R}^n} |\rho(\vec{k})|^2 d^n k}. \quad (39)$$

Therefore, the differential CE reads

$$\text{CE}_\rho = - \int \cdots \int_{\mathbb{R}^n} \rho_i(\vec{k}) \ln \rho_i(\vec{k}) d^n k, \quad (40)$$

where $\rho_i(\vec{k}) = \rho(\vec{k})/\rho_{\text{max}}(\vec{k})$

For studying pomeron resonances, one can consider $n = 1$, corresponding to the z bulk dimension. Using the Lagrangian, L , of the glueball action (23), into the stress-energy-momentum tensor

$$T^{\mu\nu} = \frac{2}{\sqrt{-g}} \left[\partial_{g_{\mu\nu}}(\sqrt{-g}L) - \partial_{x^\alpha} \partial_{\frac{\partial g_{\mu\nu}}{\partial x^\alpha}}(\sqrt{-g}L) \right], \quad (41)$$

and the $\rho(z)$ energy density, to be used in Eqs. (38 – 40), is given by the following expression,

$$\rho(z) = T_{00}(z) = \frac{1}{\zeta_s(z)^2} \left[(\mathcal{G}'(z))^2 + M_5^2(\mathcal{G}(z))^2 \right]. \quad (42)$$

Since the pomeron family has an energy density associated with, given by Eq. (42), another method for computing the pomerons mass spectra, using the CE, can be then implemented. For it, an hybrid model, that takes into account both the lattice QCD model and AdS/QCD, will be employed to derive the mass spectra of higher spin resonances in the pomeron family.

A. Hybridizing lattice QCD data, up to $J^{PC} = 6$, and AdS/QCD

The CE of pomerons, for the six dilaton models, can be numerically computed. As a first analysis, the CE of pomerons can be derived as a function of J^{PC} , by Eqs. (38 – 40), when one considers lattice QCD data, up to $J^{PC} = 6$, and including for $J^{PC} = 8, 10$ the pomeron mass spectra (30). The results are compiled in Table VII.

Data in Table VII can be then interpolated, to obtain the first type of configurational-entropic (CE) Regge trajectory, relating the CE of pomeron resonances to their J^{PC} spin. Firstly, the expression of the CE Regge trajectory, for the anomalous quadratic dilaton I model, reads

$$\text{CE}_{\text{AQD I}}(J^{PC}) = 0.02329 (J^{PC})^3 + 0.39750 (J^{PC})^2 - 0.34629 J^{PC} + 1.27524. \quad (43)$$

J^{PC}	CE _{AQD I}	CE _{AED I}	CE _{ALD I}	CE _{AQD II}	CE _{AED II}	CE _{ALD II}
0	1.00	1.10	0.88	1.30	0.92	0.81
2	2.98	3.35	2.43	3.66	2.62	2.30
4	7.82	8.72	6.02	9.32	6.62	5.42
6	18.32	22.72	13.32	25.81	15.21	14.39
8	34.78	40.92	27.72	43.99	31.08	29.18
10	62.34	72.55	48.90	76.94	53.14	51.01
12	94.62	111.16	79.95	117.46	86.11	82.12
14	138.27	162.59	121.99	170.59	129.91	124.05
16	192.92	227.17	176.83	236.96	186.82	178.27
18	259.71	306.28	317.90	246.16	258.46	246.38

TABLE VII: The CE of pomerons as a function of J^{PC} , taking into account lattice QCD data, up to $J^{PC} = 6$, and AdS/QCD, for $J^{PC} = 8, 10$. The second [fifth] column displays the pomerons CE for the anomalous quadratic dilaton I [II] (AQD I [II]) model; the third [sixth] column shows the pomerons CE computed from the anomalous exponential dilaton I [II] (AED I [II]) model; the fourth [seventh] column illustrates the CE of the pomeron family in the anomalous linear dilaton I [II] (ALD I [II]) model.

It corresponds to the dashed interpolating curve in Fig. 8. Cubic interpolation suffices to delimit accuracy within 0.42%. Besides, a similar CE Regge trajectory can be derived, in the anomalous exponential dilaton I model, representing the continuous interpolating curve in Fig. 8, as

$$\text{CE}_{\text{AED I}}(J^{PC}) = 0.028715 (J^{PC})^3 + 0.43693 (J^{PC})^2 - 0.22849 J^{PC} + 1.36214, \quad (44)$$

within 0.37% of accuracy. Analogously, the light-gray dotted CE Regge trajectory, for the anomalous linear dilaton I model, interpolates the cyan points in Fig. 8, and is given by

$$\text{CE}_{\text{ALD I}}(J^{PC}) = 0.0328785 (J^{PC})^3 + 0.15853 (J^{PC})^2 + 0.12701 J^{PC} + 0.98093, \quad (45)$$

with accuracy within 0.23%.

The expression of the CE Regge trajectory, for the anomalous quadratic dilaton II model, interpolates the black points in Fig. 8, and yields

$$\text{CE}_{\text{AQD II}}(J^{PC}) = 0.0354513 (J^{PC})^3 + 0.13899 (J^{PC})^2 + 0.31736 J^{PC} + 0.95238, \quad (46)$$

having accuracy within 0.18%. Moreover, the CE Regge trajectory in the anomalous exponential dilaton II model, is represented by the large-dashed light-gray curve that interpolates gray points, in Fig. 8,

$$\text{CE}_{\text{AED II}}(J^{PC}) = 0.028021 (J^{PC})^3 + 0.47771 (J^{PC})^2 - 0.09083 J^{PC} + 1.34452, \quad (47)$$

within 1.83% of accuracy. The black dotted CE Regge trajectory for the anomalous linear dilaton II model interpolates the orange points in Fig. 8, reading

$$\text{CE}_{\text{ALD II}}(J^{PC}) = 0.035483 (J^{PC})^3 + 0.10871 (J^{PC})^2 + 0.17159 J^{PC} + 0.91878. \quad (48)$$

Cubic interpolation delimits accuracy within $\sim 0.2\%$.

Both data in Table VII and the first type of CE Regge trajectories (43 – 48) are together displayed in Fig. 8.

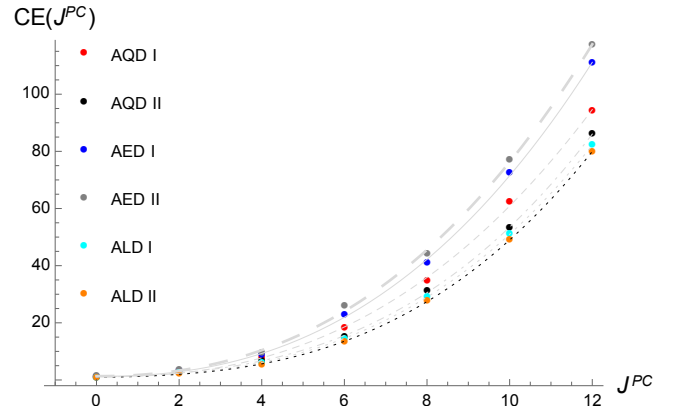


FIG. 8: CE of the pomerons as a function of J^{PC} . The anomalous quadratic dilaton I (AQD I) model is shown by the red points, whose interpolation continuous curve is given by Eq. (43), whereas the anomalous exponential dilaton I (AED I) model is illustrated by the blue points, having the dashed interpolation curve represented by Eq. (44). The anomalous linear dilaton I (ALD I) model is described by cyan points, and inset by the light-gray dotted curve, described by Eq. (45). The anomalous quadratic dilaton II (AQD II) model is shown by the black points and is interpolated by the dot-dashed light-gray curve, described by Eq. (46). The anomalous exponential dilaton II (AED II) model is illustrated by the gray points, with large-dashed interpolation curve plot by Eq. (47). The anomalous linear dilaton II (ALD II) model is depicted by orange points, with interpolation shown by the black dotted curve, described by Eq. (48).

Higher J^{PC} pomeron resonances can, thus, have their CE extrapolated from the CE Regge trajectories (43 – 48), respectively for each dilaton model.

Among the six dilaton models, Fig. 8 shows that the anomalous exponential dilaton II model represents more configurationally unstable states, whereas the anomalous linear dilaton II model regards pomeron resonances that are more stable, from the configurational point of view.

For deriving the pomeron mass spectra in the six dilatonic models, we will first use, for the pomeron mass spectra up to $J^{PC} = 6$, the third column of Table I. In fact, it encompasses an average derivation from lattice QCD, including both a finite range of N_c and $N_c \rightarrow \infty$. Therefore, we use just the available data up to $J^{PC} = 6$, from QCD lattice setups, completing for $J^{PC} = 8, 10$ the pomeron mass spectra obtained from AdS/QCD (30).

This is displayed in the second column of Table I. Therefore, the interpolation fitting of the point, representing the CE as a function of the pomeron mass spectra, will provide the mass spectra of the next generation of pomeron resonances, with $J^{PC} = 12, 14, 16, 18, \dots$

The CE Regge trajectory, relating the CE to the pomerons (squared) mass spectra, is shown in Fig. 9.

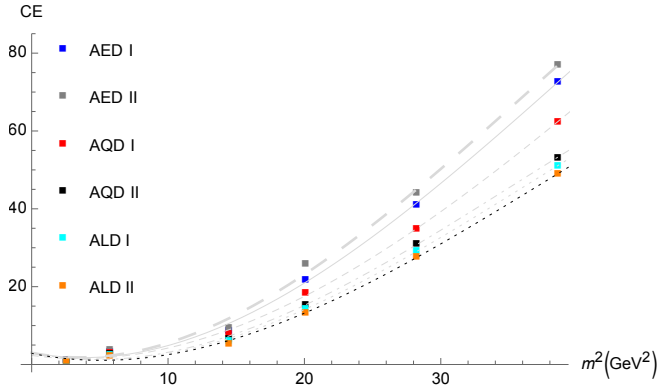


FIG. 9: CE of the pomeron family, with respect to the squared mass spectra, taking into account exclusively lattice QCD data, up to $J^{PC} = 6$, and including, for $J^{PC} = 8, 10$, the pomeron mass spectra (30). The anomalous quadratic dilaton I [II] model is shown by the red [black] boxes, whereas the anomalous exponential dilaton I [II] model is illustrated by the blue [gray] boxes; the anomalous linear dilaton I [II] model is depicted by cyan [orange] boxes.

Higher J^{PC} pomeron resonances will have their CE extrapolated from the CE Regge trajectories (43, 49) and (46, 64), for the anomalous quadratic dilaton I and II models, respectively; from the CE Regge trajectories (44, 54) and (47, 69), respectively for the anomalous exponential dilaton I and II models; and from Eqs. (45, 59) and (48, 74), respectively, for the anomalous linear dilaton I and II models.

The dashed CE Regge trajectory in Fig. 9 corresponds to Eq. (49), that interpolates the mass spectra of pomerons for the anomalous quadratic dilaton I model,

$$\text{CE}_{\text{AQD I}}(m) = -0.0004947m^6 + 0.0719030m^4 - 0.4808326m^2 + 2.3348292, \quad (49)$$

within 0.25% standard deviation. This hybrid model, taking into account lattice QCD data up $J^{PC} = 6$ and including, for $J^{PC} = 8, 10$, the pomeron mass spectra (30), yields the mass spectra of the $\mathcal{P}_{12}, \mathcal{P}_{14}, \mathcal{P}_{16}$ and \mathcal{P}_{18} pomeron resonances, by employing Eqs. (43, 49). In fact, for $J^{PC} = 12$, Eq. (43) yields $\text{CE} = 94.6198$. Then substituting this value in the CE Regge trajectory (49), and solving the resulting cubic algebraic equation, the solution is the mass of the \mathcal{P}_{12} pomeron, given by

$$m_{\mathcal{P}_{12}} = 7.0334 \text{ GeV}. \quad (50)$$

Similarly for the next pomeron resonances \mathcal{P}_{14} , substituting $J^{PC} = 14$ into Eq. (43) implies that the corre-

sponding CE equals to 138.269. Hence, replacing this value into the CE Regge trajectory (49) yields

$$m_{\mathcal{P}_{14}} = 8.0445 \text{ GeV}. \quad (51)$$

Besides, the same protocol can be accomplished for the \mathcal{P}_{16} pomeron, when Eq. (43) implies that $\text{CE}_{\mathcal{P}_{16}} = 192.926$. When reinstated in Eq. (49), it produces the mass, for the \mathcal{P}_{16} pomeron,

$$m_{\mathcal{P}_{16}} = 9.7421 \text{ GeV}. \quad (52)$$

Analogously, for the \mathcal{P}_{18} , we compute $\text{CE}_{\mathcal{P}_{18}} = 259.712$, and reinstating into Eq. (49), it produces the \mathcal{P}_{18} pomeron mass

$$m_{\mathcal{P}_{18}} = 10.1372 \text{ GeV}. \quad (53)$$

Besides, the continuous curve in Fig. 9, that interpolates the blue boxes that fit the mass spectra of pomerons, when the anomalous exponential dilaton I model is employed, is given by

$$\text{CE}_{\text{AED I}}(m) = -0.00079069m^6 + 0.09515m^4 - 0.69436m^2 + 3.08280, \quad (54)$$

within 0.98% standard deviation. For $J^{PC} = 12$, Eq. (44) yields $\text{CE}_{\mathcal{P}_{12}} = 111.1588$. Then substituting this value into the CE Regge trajectory (54), solving the resulting equation yields the solution

$$m_{\mathcal{P}_{12}} = 7.1628 \text{ GeV}, \quad (55)$$

for the \mathcal{P}_{12} pomeron mass. Similarly, for the pomeron \mathcal{P}_{14} , substituting $J^{PC} = 14$ into Eq. (44) implies that $\text{CE}_{\mathcal{P}_{14}} = 162.597$. Hence, replacing it into the CE Regge trajectory (54) yields

$$m_{\mathcal{P}_{14}} = 8.8109 \text{ GeV}. \quad (56)$$

Employing a similar procedure for the \mathcal{P}_{16} pomeron, Eq. (44) for $J^{PC} = 16$ yields $\text{CE}_{\mathcal{P}_{16}} = 227.179$. When replaced into Eq. (54), it produces the mass, for the \mathcal{P}_{16} pomeron,

$$m_{\mathcal{P}_{16}} = 9.2062 \text{ GeV}, \quad (57)$$

and respectively for the \mathcal{P}_{18} element, $\text{CE}_{\mathcal{P}_{18}} = 306.284$, and reinstating into Eq. (54), it produces the \mathcal{P}_{18} pomeron mass

$$m_{\mathcal{P}_{18}} = 9.5809 \text{ GeV}. \quad (58)$$

Now we analyze the anomalous linear dilaton I model, whose CE Regge trajectory is given by

$$\text{CE}_{\text{ALD I}}(m) = -0.000708092m^6 + 0.078713m^4 - 0.73749m^2 + 3.05330, \quad (59)$$

within 0.83% standard deviation. When one fixes $J^{PC} = 12$, Eq. (45) yields $\text{CE} = 82.117$. Therefore, this value is

reinstated in the CE Regge trajectory (59), and solving the resulting equation, the solution is the mass

$$m_{\mathcal{P}_{12}} = 7.3861 \text{ GeV}, \quad (60)$$

for the \mathcal{P}_{12} pomeron. It yields a reliable range $7.35 \text{ GeV} \lesssim m_{\mathcal{P}_{12}} \lesssim 7.42 \text{ GeV}$. Similarly for the next pomeron resonance, \mathcal{P}_{14} , substituting $J^{PC} = 14$ into Eq. (46) implies that the CE equals 124.049. Replacing it into the CE Regge trajectory (59) yields

$$m_{\mathcal{P}_{14}} = 8.6039 \text{ GeV}, \quad (61)$$

being the range $8.58 \text{ GeV} \lesssim m_{\mathcal{P}_{14}} \lesssim 8.62 \text{ GeV}$ trustworthy. A similar procedure is used for the \mathcal{P}_{16} pomeron, when Eq. (45) implies that $\text{CE}_{\mathcal{P}_{16}} = 178.267$, for $J^{PC} = 16$. When reinstated in Eq. (59), it yields the mass

$$m_{\mathcal{P}_{16}} = 9.0158 \text{ GeV}. \quad (62)$$

Now, replacing $J^{PC} = 18$ in Eq. (45) implies that the corresponding CE has value 246.378. Therefore, solving for it, Eq. (64) yields

$$m_{\mathcal{P}_{18}} = 9.4091 \text{ GeV}. \quad (63)$$

The CE Regge trajectory interpolating curve, corresponding to the anomalous quadratic dilaton II model reads

$$\begin{aligned} \text{CE}_{\text{AQD II}}(m) = & -0.00078764m^6 + 0.083448m^4 \\ & -0.74445m^2 + 3.01507, \end{aligned} \quad (64)$$

within 0.79% standard deviation. The mass spectra for the $\mathcal{P}_{12}, \mathcal{P}_{14}, \mathcal{P}_{16}$ and \mathcal{P}_{18} pomeron resonances can be straightforwardly deduced, when one uses Eqs. (46, 64). In fact, for $J^{PC} = 12$, Eq. (46) yields $\text{CE} = 86.035$. Then substituting this value in (64), and solving the resulting equation, the solution is the mass

$$m_{\mathcal{P}_{12}} = 7.5618 \text{ GeV}. \quad (65)$$

It yields a reliable range $7.54 \text{ GeV} \lesssim m_{\mathcal{P}_{12}} \lesssim 7.58 \text{ GeV}$. Similarly for the next pomeron resonance \mathcal{P}_{14} , substituting $J^{PC} = 14$ into Eq. (46) implies the CE equals 129.916. Hence, replacing this value into the CE Regge trajectory (64) yields

$$m_{\mathcal{P}_{14}} = 8.4893 \text{ GeV}, \quad (66)$$

being the mass range $8.51 \text{ GeV} \lesssim m_{\mathcal{P}_{14}} \lesssim 8.47 \text{ GeV}$ a sound one. A similar procedure is used for the \mathcal{P}_{16} pomeron, when Eq. (46) implies that $\text{CE}_{\mathcal{P}_{16}} = 186.8200$. When reinstated in Eq. (64), it yields the mass

$$m_{\mathcal{P}_{16}} = 8.8991 \text{ GeV}. \quad (67)$$

Now, replacing $J^{PC} = 18$ in Eq. (46) implies that the corresponding CE has value 258.4495. Therefore, solving Eq. (64) with this value yields

$$m_{\mathcal{P}_{18}} = 9.2907 \text{ GeV}. \quad (68)$$

The CE Regge trajectory interpolating curve, corresponding to the anomalous exponential dilaton II model reads

$$\begin{aligned} \text{CE}_{\text{AED II}}(m) = & -0.000929376 + 0.103323m^4 \\ & -0.688707m^2 + 3.01135, \end{aligned} \quad (69)$$

within 0.89% standard deviation. Now, for $J^{PC} = 12$, Eq. (47) yields $\text{CE} = 117.46$. Therefore, when one replaces it into (69), it yields mass

$$m_{\mathcal{P}_{12}} = 7.2542 \text{ GeV}. \quad (70)$$

In a similar way, for the next pomeron resonance \mathcal{P}_{14} , substituting $J^{PC} = 14$ into Eq. (47) implies that the CE has value 170.593. Hence, replacing this value into (49) yields

$$m_{\mathcal{P}_{14}} = 8.60425 \text{ GeV}. \quad (71)$$

An analogous procedure is used for the \mathcal{P}_{16} pomeron, when Eq. (47) implies that $\text{CE}_{\mathcal{P}_{16}} = 236.957$. When reinstated in Eq. (69), it yields the mass

$$m_{\mathcal{P}_{16}} = 8.98653 \text{ GeV}. \quad (72)$$

Now, replacing $J^{PC} = 18$ in Eq. (47) implies that the CE has value 317.905. Therefore, solving for it Eq. (69) yields

$$m_{\mathcal{P}_{18}} = 9.3489 \text{ GeV}. \quad (73)$$

Now, the last model to be analyzed is the anomalous linear dilaton II model, whose CE Regge trajectory is given by

$$\begin{aligned} \text{CE}_{\text{ALD II}}(m) = & -0.00064434m^6 + 0.0743293m^4 \\ & -0.71216m^2 + 2.85792, \end{aligned} \quad (74)$$

within 0.83% standard deviation. When one fixes $J^{PC} = 12$, Eq. (48) yields $\text{CE} = 79.945$. Therefore, Eq. (74) yields

$$m_{\mathcal{P}_{12}} = 7.3589 \text{ GeV}. \quad (75)$$

Similarly for the next member \mathcal{P}_{14} of the pomeron family, substituting $J^{PC} = 14$ into Eq. (48) implies that the CE equals 121.990. Consequently, replacing this value into (74) yields

$$m_{\mathcal{P}_{14}} = 8.7266 \text{ GeV}. \quad (76)$$

A similar protocol is utilized for the \mathcal{P}_{16} pomeron, when Eq. (48) implies that $\text{CE}_{\mathcal{P}_{16}} = 176.836$. When reinstated in Eq. (74), it yields the mass

$$m_{\mathcal{P}_{16}} = 9.1537 \text{ GeV}. \quad (77)$$

Now, replacing $J^{PC} = 18$ in Eq. (48) implies that the corresponding CE has value 246.161. Therefore, solving for it Eq. (74) yields

$$m_{\mathcal{P}_{18}} = 9.5615 \text{ GeV}. \quad (78)$$

The mass spectra of pomerons as a function of the pomeron mass m (GeV), taking into account exclusively lattice QCD data up to $J^{PC} = 6$, and including for $J^{PC} = 8, 10$ the pomeron mass spectra (30) of AdS/QCD, in the six dilaton models, are summarized in Table VIII.

J^{PC}	$m_{\text{AQD I}}$	$m_{\text{AED I}}$	$m_{\text{ALD I}}$	$m_{\text{AQD II}}$	$m_{\text{AED II}}$	$m_{\text{ALD II}}$
12	7.03	7.16	7.38	7.56	7.25	7.35
14	8.04	8.81	8.60	8.48	8.60	8.72
16	9.74	9.21	9.01	8.90	8.98	9.15
18	10.14	9.58	9.40	9.29	9.34	9.56

TABLE VIII: Mass spectra (GeV) of pomerons as a function of J^{PC} , taking into account exclusively lattice QCD data up to $J^{PC} = 6$, and including for $J^{PC} = 8, 10$ the pomeron mass spectra (30). The second and fifth columns display the CE of the anomalous quadratic dilaton I and II (AQD I and II) models; the third and sixth columns show the pomerons CE computed from the anomalous exponential dilaton I and II (AED I and II) models; the fourth and seventh columns depict the CE computed from the anomalous linear dilaton I and II (ALD I and II) models.

B. Using just lattice QCD data up to $J^{PC} = 6$

Now, using exclusively the available data up to $J^{PC} = 6$, from lattice QCD data, the CE of the pomeron family can be computed by Eqs. (38 – 40).

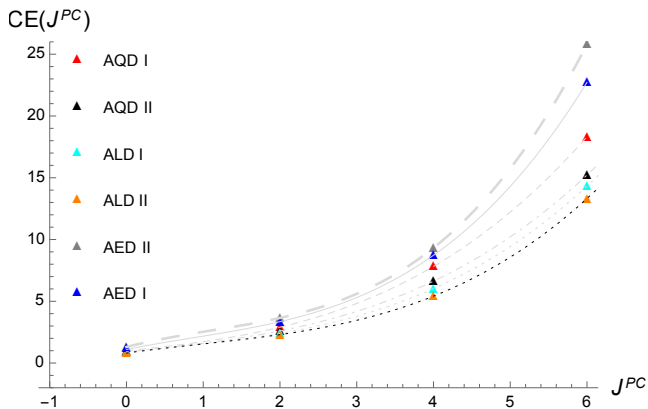


FIG. 10: CE of the pomeron family with respect to J^{PC} , taking into account exclusively lattice QCD data, up to $J^{PC} = 6$. The anomalous quadratic dilaton I [II] model is shown by red [black] triangles, whereas the anomalous exponential dilaton I [II] model is illustrated by blue [gray] triangles; and the anomalous linear dilaton I [II] model is depicted by cyan [orange] triangles.

For the anomalous quadratic dilaton I model, the first type of CE Regge trajectory, when one considers exclusively the available lattice QCD data up to $J^{PC} = 6$ from

lattice QCD, reads

$$\text{CE}_{\text{AQD I}}(J^{PC}) = 0.05333 (J^{PC})^3 + 0.05750 (J^{PC})^2 + 0.62166 J^{PC} + 0.99999. \quad (79)$$

It is the dashed light-gray curve in Fig. 10, that interpolates red triangles with accuracy within 0.11%. Besides, the expression of the CE Regge trajectory for the anomalous exponential dilaton I model, representing the continuous curve, that interpolates blue triangles in Fig. 10, is given by

$$\text{CE}_{\text{AED I}}(J^{PC}) = 0.11479 (J^{PC})^3 - 0.29874 (J^{PC})^2 + 1.26333 J^{PC} + 1.09999. \quad (80)$$

The formula of the CE Regge trajectory, for the anomalous linear dilaton I model, reads

$$\text{CE}_{\text{ALD I}}(J^{PC}) = 0.05352 (J^{PC})^3 - 0.05850 (J^{PC})^2 + 0.66241 J^{PC} + 0.88099. \quad (81)$$

It corresponds to the dotted curve, interpolating cyan triangles in Fig. 8, with accuracy within 0.21%.

The expression of the CE Regge trajectory, for the anomalous quadratic dilaton II model, reads

$$\text{CE}_{\text{AQD II}}(J^{PC}) = 0.046875 (J^{PC})^3 + 0.008749 (J^{PC})^2 + 0.645 J^{PC} + 0.900. \quad (82)$$

It corresponds to the light-gray dot-dashed curve, interpolating black triangles in Fig. 8. Cubic interpolation suffices to delimit accuracy within $\sim 0.19\%$. Besides, the expression of the CE Regge trajectory for the anomalous exponential dilaton II model, representing the large-dashed light-gray interpolating curve in Fig. 10, is given by

$$\text{CE}_{\text{AED II}}(J^{PC}) = 0.15625 (J^{PC})^3 - 0.5225 (J^{PC})^2 + 1.5950 J^{PC} + 1.300. \quad (83)$$

It has accuracy of 0.13%. Finally, the formula of the CE Regge trajectory, for the anomalous linear dilaton II model, reads

$$\text{CE}_{\text{ALD II}}(J^{PC}) = 0.0660208 (J^{PC})^3 - 0.1935 (J^{PC})^2 + 0.86741 J^{PC} + 0.81100. \quad (84)$$

It corresponds to the black dotted curve, interpolating orange triangles, in Fig. 8, with accuracy within $\sim 0.8\%$.

It is worth to mention that, for the anomalous linear models, there are several possibilities that best fit the QCD lattice pomeron mass spectra, for low J^{PC} . Hence, some appropriate choices for 2-tuple (k, γ_0) can be employed for matching QCD lattice predictions regarding the pomeron family. Some values best fit the $J^{PC} = 0^{++}, 2^{++}$ pomerons, whereas other values of

(k, γ_0) best fit higher J^{PC} pomeron resonances. For different values of k and γ_0 , the CE of the pomerons with respect to J^{PC} is plot in Fig. 11.

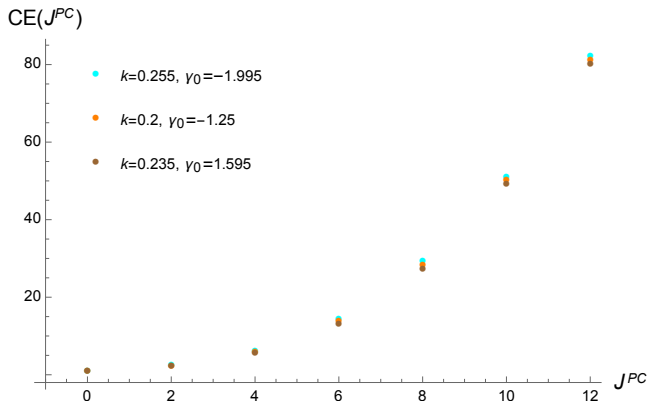


FIG. 11: CE of the pomeron family with respect to J^{PC} , for different values of k and γ_0 , in the anomalous linear model I. Cyan points represent $k = 0.255$ and $\gamma_0 = -1.995$; orange points depict the case $k = 0.2$ and $\gamma_0 = -1.25$; and brown points represent $k = 0.235$ and $\gamma_0 = 1.595$.

Since the three appropriate choices of (k, γ_0) , studied and illustrated in Fig. 11, generate the respective CEs, with a maximum variance of 1.1%, it indicates that they present approximately equal configurational stability. Hence, this is the reason we chose $k = 0.255$ and $\gamma_0 = -1.995$ in all the analysis regarding the anomalous linear dilaton I model.

When one attributes values $J^{PC} = 8, 10, \dots, 18$ in the CE Regge trajectories (79, 80, 82), respectively for the six dilaton models, the CE of the pomeron family are compiled, in the second to the seventh columns of Table IX.

J^{PC}	CE _{AQD I}	CE _{AED I}	CE _{ALD I}	CE _{AQD II}	CE _{AED II}	CE _{ALD II}
0	1.00	1.10	0.88	0.92	1.30	0.81
2	2.99	3.35	2.30	2.62	3.66	2.43
4	7.82	8.72	5.42	6.62	9.32	6.02
6	18.32	22.73	13.32	15.21	25.81	14.31
8	36.96	50.86	28.97	30.62	60.62	27.41
10	66.34	98.65	50.98	55.12	121.25	48.99
12	108.93	171.63	82.14	90.94	215.20	79.94
14	167.32	275.22	124.05	140.27	349.97	121.99
16	244.13	415.02	178.26	205.46	533.06	176.83
18	341.87	596.52	246.38	288.72	771.97	246.16

TABLE IX: The CE of pomerons as a function of J^{PC} , taking into account exclusively lattice QCD data up to $J^{PC} = 6$. The second and fifth columns display the CE of the anomalous quadratic dilaton I and II (AQD I and II) models; the third and sixth columns show the pomerons CE computed from the anomalous exponential dilaton I and (AED I and II) models; the fourth and seventh columns show the CE, respectively computed from the anomalous linear dilaton I and II (ALD I and II) models.

Similarly for the hybrid model shown in Fig. 8, also Fig. 10 illustrates that the anomalous exponential dilaton I model regards pomeron resonances that are configurationally more unstable states, when compared with other dilaton models. Again, the anomalous linear dilaton I model does designate pomeron resonances that are more stable, from the configurational point of view.

Now, with the pomeron family mass spectra, for $J^{PC} = 0, 2, 4, 6$, obtained from lattice QCD, higher spin pomeron resonances can have their masses determined, when a second type of CE Regge trajectories is considered. They interpolate the plot of the pomeron family, for $J^{PC} = 0, 2, 4, 6$, with respect to their mass spectra, for the six dilaton models, and displayed in Fig. 12.

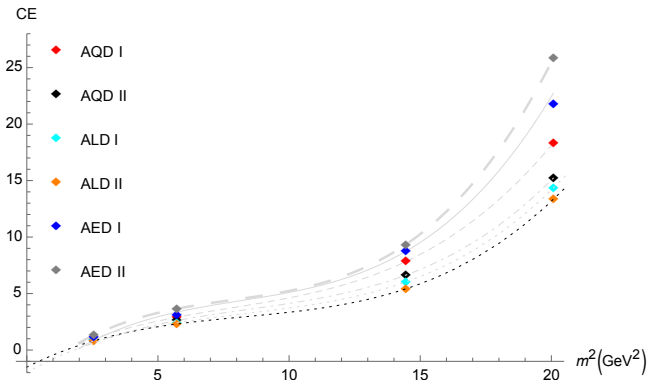


FIG. 12: CE of the pomeron family with respect to their mass spectra, taking into account exclusively lattice QCD data, up to $J^{PC} = 6$. The anomalous quadratic dilaton I [II] model is shown by the red [black] diamonds, whereas the anomalous exponential dilaton I [II] model is illustrated by the blue [gray] diamonds; and the anomalous linear dilaton I [II] model is depicted by cyan [orange] diamonds.

Higher J^{PC} pomeron resonances will have their mass spectrum, therefore, extrapolated from Eqs. (79, 85), for the anomalous quadratic dilaton I model; from Eqs. (80, 92), for the anomalous exponential dilaton I model; from Eqs. (82, 106), for the anomalous quadratic dilaton model; and from Eqs. (81, 99) and (84, 120), respectively for the anomalous linear dilaton I and II models.

Therefore the CE of pomerons with respect to the (squared) mass spectra, for the anomalous quadratic dilaton I model, is shown by the dashed curve in Fig. 12, that interpolates the red diamonds, reading

$$\begin{aligned} \text{CE}_{\text{AQD I}}(m) = & 0.00534334m^6 - 0.1243014m^4 \\ & + 1.339408m^2 - 1.690979, \end{aligned} \quad (85)$$

within 0.78% standard deviation. For obtaining the mass spectra of the higher spin resonances in the pomeron family, let us first analyze the CE Regge trajectory (85), also derived from the anomalous quadratic dilaton I model. In fact, choosing for $J^{PC} = 8$, Eq. (79) yields $\text{CE} = 36.961$. When this value is replaced in the CE Regge trajectory (85), it yields the mass

$$m_{\mathcal{P}_8} = 4.9875 \text{ GeV} \quad (86)$$

It yields a reliable range $5.00 \text{ GeV} \lesssim m_{\mathcal{P}_8} \lesssim 4.96 \text{ GeV}$. Analogously, when one substitutes $J^{PC} = 10$ into Eq. (79), it yields the CE equal to 66.30. Putting back in Eq. (85) produces

$$m_{\mathcal{P}_{10}} = 5.4253 \text{ GeV}, \quad (87)$$

being the mass range $5.44 \text{ GeV} \lesssim m_{\mathcal{P}_{10}} \lesssim 5.48 \text{ GeV}$ a reliable one. For the \mathcal{P}_{12} pomeron, the CE Regge trajectory (79) yields $\text{CE}_{\mathcal{P}_{12}} = 108.98$, when $J^{PC} = 12$ is taken into account. When reinstated in Eq. (85), the mass

$$m_{\mathcal{P}_{12}} = 5.8214 \text{ GeV} \quad (88)$$

is then derived. Similarly, replacing $J^{PC} = 14$ in Eq. (79) implies $\text{CE}_{\mathcal{P}_{14}} = 167.32$. Consequently, when one solves Eq.(85) for this value, it implies that

$$m_{\mathcal{P}_{14}} = 6.1879 \text{ GeV}. \quad (89)$$

In the same way, the CE Regge trajectory (79) yields $\text{CE}_{\mathcal{P}_{16}} = 244.12$, when $J^{PC} = 16$ is taken into account. When reinstated in Eq. (85), the mass

$$m_{\mathcal{P}_{16}} = 6.5316 \text{ GeV} \quad (90)$$

is derived. Moreover, the value $J^{PC} = 18$ is associated to $\text{CE}_{\mathcal{P}_{18}} = 341.86$ that can be replaced in Eq. (85), producing

$$m_{\mathcal{P}_{18}} = 6.8568 \text{ GeV}. \quad (91)$$

These results are compiled in the second column in Table X.

The CE Regge trajectory, that interpolates the CE of the pomeron family, for $J^{PC} = 0, 2, 4, 6$, to the pomerons (squared) mass spectra, is shown by the continuous curve in Fig. 12, for the anomalous exponential dilaton I,

$$\begin{aligned} \text{CE}_{\text{AED I}}(m) = & 0.00829209m^6 - 0.203204m^4 \\ & + 2.026744m^2 - 3.142225, \end{aligned} \quad (92)$$

within 0.4% standard deviation. For the anomalous exponential dilaton I model, in fact, choosing for $J^{PC} = 8$, Eq. (80) yields $\text{CE} = 50.863$. When this value is replaced in the CE Regge trajectory (92), it yields the mass

$$m_{\mathcal{P}_8} = 5.0103 \text{ GeV}, \quad (93)$$

for the \mathcal{P}_8 pomeron. It yields a reliable range $4.99 \text{ GeV} \lesssim m_{\mathcal{P}_8} \lesssim 5.03 \text{ GeV}$. Analogously, for when one substitutes $J^{PC} = 10$ into Eq. (80) yields the CE equal to 98.652. Putting back in Eq. (92) produces

$$m_{\mathcal{P}_{10}} = 5.4772 \text{ GeV}, \quad (94)$$

being the mass range $5.45 \text{ GeV} \lesssim m_{\mathcal{P}_{10}} \lesssim 5.50 \text{ GeV}$. A similar calculation can be employed for the \mathcal{P}_{12} pomeron. Indeed, the CE Regge trajectory (79) yields $\text{CE}_{\mathcal{P}_{12}} = 171.63$, when $J^{PC} = 12$ is taken into account. When reinstated in Eq. (85), the mass

$$m_{\mathcal{P}_{12}} = 5.9035 \text{ GeV} \quad (95)$$

is derived. Similarly, replacing $J^{PC} = 14$ in Eq. (79) implies $\text{CE}_{\mathcal{P}_{14}} = 275.22$. Consequently, when one solves Eq.(85) for this value, it implies that

$$m_{\mathcal{P}_{14}} = 6.2991 \text{ GeV}. \quad (96)$$

In the same way, the CE Regge trajectory (79) yields $\text{CE}_{\mathcal{P}_{16}} = 415.02$, when $J^{PC} = 16$ is taken into account. When reinstated in Eq. (85), the mass

$$m_{\mathcal{P}_{16}} = 6.6708 \text{ GeV} \quad (97)$$

is derived. Moreover, the value $J^{PC} = 18$ is associated to $CE_{\mathcal{P}_{18}} = 596.52$ that can be replaced in Eq. (85), yielding

$$m_{\mathcal{P}_{18}} = 7.0214 \text{ GeV}. \quad (98)$$

The derived mass spectra for this dilaton model is displayed in the third column of Table X.

Respectively, for the anomalous linear dilaton I model, the CE values of the pomeron family, for $J^{PC} = 8, 10, \dots, 18$ are displayed in the fourth column of Table X. The CE Regge trajectory, interpolating the CE to the pomerons (squared) mass spectra, is displayed the dotted curve in Fig. 12, being given by

$$CE_{\text{ALDI}}(m) = 0.0048877 m^6 - 0.12293 m^4 + 1.31044 m^2 - 1.98507, \quad (99)$$

within 0.1% standard deviation. Choosing for $J^{PC} = 8$, Eq. (81) yields $CE = 28.9767$. Now, replacing this value in (99) yields the mass

$$m_{\mathcal{P}_8} = 4.96854 \text{ GeV}, \quad (100)$$

for the \mathcal{P}_8 pomeron. It yields a reliable range $4.94 \text{ GeV} \lesssim m_{\mathcal{P}_8} \lesssim 4.98 \text{ GeV}$. Analogously, substituting $J^{PC} = 10$ into Eq. (81) yields the CE equal to 50.982. Putting back in Eq. (99) produces

$$m_{\mathcal{P}_{10}} = 5.37295 \text{ GeV}, \quad (101)$$

being the mass range $5.35 \text{ GeV} \lesssim m_{\mathcal{P}_{10}} \lesssim 5.39 \text{ GeV}$. The CE Regge trajectory (81) yields $CE_{\mathcal{P}_{12}} = 82.1473$, when $J^{PC} = 12$ is taken into account. When reinstated in Eq. (99), the mass

$$m_{\mathcal{P}_{12}} = 5.7361 \text{ GeV} \quad (102)$$

is derived. Similarly, replacing $J^{PC} = 14$ in Eq. (81) implies $CE_{\mathcal{P}_{14}} = 124.049$. Consequently, when one solves Eq. (99) for this value, it implies that

$$m_{\mathcal{P}_{14}} = 6.07114 \text{ GeV}. \quad (103)$$

In the same way, the CE Regge trajectory (81) yields $CE_{\mathcal{P}_{16}} = 178.267$, when $J^{PC} = 16$ is taken into account. When reinstated in Eq. (99), the mass

$$m_{\mathcal{P}_{16}} = 6.38486 \text{ GeV} \quad (104)$$

is derived. Moreover, the value $J^{PC} = 18$ is associated to $CE_{\mathcal{P}_{18}} = 246.378$ that can be replaced in Eq. (99), yielding

$$m_{\mathcal{P}_{18}} = 6.68154 \text{ GeV}. \quad (105)$$

Besides, the CE Regge trajectory, interpolating the CE to the pomerons (squared) mass spectra, is displayed the dot-dashed curve in Fig. 12, for the anomalous quadratic II dilaton,

$$CE_{\text{AQD II}}(m) = 0.0050079 m^6 - 0.12725 m^4 + 1.40438 m^2 - 2.20316, \quad (106)$$

within 0.2% standard deviation. In fact, choosing for $J^{PC} = 8$, Eq. (82) yields $CE = 30.621$. When this value is replaced in the CE Regge trajectory (106), it yields the mass

$$m_{\mathcal{P}_8} = 4.9771 \text{ GeV}, \quad (107)$$

for the \mathcal{P}_8 pomeron. It yields a reliable range $4.94 \text{ GeV} \lesssim m_{\mathcal{P}_8} \lesssim 4.99 \text{ GeV}$. When substituting $J^{PC} = 10$ into Eq. (82) yields the CE equal to 55.123 and replacing in Eq. (106) yields

$$m_{\mathcal{P}_{10}} = 5.4056 \text{ GeV}, \quad (108)$$

being the mass range $5.37 \text{ GeV} \lesssim m_{\mathcal{P}_{10}} \lesssim 5.43 \text{ GeV}$. Now, the CE Regge trajectory (82) yields $CE_{\mathcal{P}_{12}} = 90.945$, when $J^{PC} = 12$ is taken into account. When placed in Eq. (106), the mass

$$m_{\mathcal{P}_{12}} = 5.7935 \text{ GeV} \quad (109)$$

is derived. Similarly, replacing $J^{PC} = 14$ in Eq. (82) implies $CE_{\mathcal{P}_{14}} = 140.279$. Consequently, when one solves Eq. (106) for this value, it implies that

$$m_{\mathcal{P}_{14}} = 6.1526 \text{ GeV}. \quad (110)$$

In the same way, the CE Regge trajectory (82) yields $CE_{\mathcal{P}_{16}} = 205.467$, when $J^{PC} = 16$ is taken into account. When reinstated in Eq. (106), one obtains the mass

$$m_{\mathcal{P}_{16}} = 6.4902 \text{ GeV}. \quad (111)$$

Moreover, the value $J^{PC} = 18$ is associated to $CE_{\mathcal{P}_{18}} = 288.720$ that can be replaced in Eq. (106), yielding

$$m_{\mathcal{P}_{18}} = 6.8099 \text{ GeV}. \quad (112)$$

These results are compiled in the fifth column in Table X.

The CE Regge trajectory, that interpolates the CE of the pomeron family, for $J^{PC} = 0, 2, 4, 6$, to the pomerons (squared) mass spectra, is shown by the continuous curve in Fig. 12, for the anomalous exponential dilaton II,

$$CE_{\text{AED II}}(m) = 0.00949858 m^6 - 0.223326 m^4 + 2.07616 m^2 - 2.69281, \quad (113)$$

within 0.4% standard deviation. For the anomalous exponential dilaton II model, in fact, choosing for $J^{PC} = 8$, Eq. (83) yields $CE = 60.621$. When this value is replaced in the CE Regge trajectory (113), it yields the mass

$$m_{\mathcal{P}_8} = 5.0289 \text{ GeV}, \quad (114)$$

for the \mathcal{P}_8 pomeron. It yields a reliable range $4.99 \text{ GeV} \lesssim m_{\mathcal{P}_8} \lesssim 5.03 \text{ GeV}$. Analogously, substituting $J^{PC} = 10$ into Eq. (83) yields the CE equal to 121.259. Putting back in Eq. (113) produces

$$m_{\mathcal{P}_{10}} = 5.5159 \text{ GeV}, \quad (115)$$

being the mass range $5.48 \text{ GeV} \lesssim m_{\mathcal{P}_{10}} \lesssim 5.54 \text{ GeV}$. A similar calculation can be employed for the \mathcal{P}_{12} pomeron. Indeed, the CE Regge trajectory (83) yields $\text{CE}_{\mathcal{P}_{12}} = 215.27$, when $J^{PC} = 12$ is taken into account. When reinstated in Eq. (113), the mass

$$m_{\mathcal{P}_{12}} = 5.9610 \text{ GeV} \quad (116)$$

is derived. Similarly, replacing $J^{PC} = 14$ in Eq. (79) implies $\text{CE}_{\mathcal{P}_{14}} = 349.970$. Consequently, when one solves Eq. (85) for this value, it implies that

$$m_{\mathcal{P}_{14}} = 6.3739 \text{ GeV}. \quad (117)$$

In the same way, the CE Regge trajectory (79) yields $\text{CE}_{\mathcal{P}_{16}} = 533.06$, when $J^{PC} = 16$ is taken into account. When replaced in Eq. (85), the mass

$$m_{\mathcal{P}_{16}} = 6.7614 \text{ GeV} \quad (118)$$

is derived. Moreover, the value $J^{PC} = 18$ is associated to $\text{CE}_{\mathcal{P}_{18}} = 771.97$ that can be replaced in Eq. (85), yielding

$$m_{\mathcal{P}_{18}} = 7.1277 \text{ GeV}. \quad (119)$$

The derived mass spectra of the pomeron family, for $J^{PC} = 8, 10, \dots, 18$, is displayed in the sixth column of Table X.

Respectively, for the anomalous linear dilaton II model, the CE values of the pomeron family, for $J^{PC} = 8, 10, \dots, 18$ are displayed in the fourth column of Table IX. The CE Regge trajectory, relating the pomeron mass spectra to the CE, for this model, reads

$$\begin{aligned} \text{CE}_{\text{ALD II}}(m) &= 0.00470485 m^6 - 0.116337 m^4 \\ &\quad + 1.17817 m^2 - 1.51081, \end{aligned} \quad (120)$$

within 0.4% standard deviation. Consequently, employing the same procedure using the CE Regge trajectories (84, 120), the derived mass spectra of the pomeron family, for $J^{PC} = 8, 10, \dots, 18$, is displayed in the fourth column of Table X. In fact, choosing for $J^{PC} = 8$, Eq. (84) yields $\text{CE} = 27.419$. When this value is replaced in the CE Regge trajectory (120), it yields the mass

$$m_{\mathcal{P}_8} = 4.9673 \text{ GeV}, \quad (121)$$

for the \mathcal{P}_8 pomeron. It yields a reliable range $4.94 \text{ GeV} \lesssim m_{\mathcal{P}_8} \lesssim 4.98 \text{ GeV}$. Analogously, for when one substitutes $J^{PC} = 10$ into Eq. (84) yields the CE equal to 48.990. Putting back in Eq. (120) produces

$$m_{\mathcal{P}_{10}} = 5.3767 \text{ GeV}, \quad (122)$$

being the mass range $5.35 \text{ GeV} \lesssim m_{\mathcal{P}_{10}} \lesssim 5.40 \text{ GeV}$. A similar calculation can be employed for the \mathcal{P}_{12} pomeron. Indeed, the CE Regge trajectory (84) yields $\text{CE}_{\mathcal{P}_{12}} = 79.9451$, when $J^{PC} = 12$ is taken into account. When reinstated in Eq. (120), the mass

$$m_{\mathcal{P}_{12}} = 5.7464 \text{ GeV} \quad (123)$$

is derived. Similarly, replacing $J^{PC} = 14$ in Eq. (84) implies $\text{CE}_{\mathcal{P}_{14}} = 121.993$. Consequently, when one solves Eq. (120) for this value, it implies that

$$m_{\mathcal{P}_{14}} = 6.0887 \text{ GeV}. \quad (124)$$

In the same way, the CE Regge trajectory (84) yields $\text{CE}_{\mathcal{P}_{16}} = 176.832$, when $J^{PC} = 16$ is taken into account. When reinstated in Eq. (120), the mass

$$m_{\mathcal{P}_{16}} = 6.4099 \text{ GeV} \quad (125)$$

is derived. Moreover, the value $J^{PC} = 18$ is associated to $\text{CE}_{\mathcal{P}_{18}} = 246.167$ that can be replaced in Eq. (120), yielding

$$m_{\mathcal{P}_{18}} = 6.71401 \text{ GeV}. \quad (126)$$

is derived. These results are compiled in the seventh column in Table X.

J^{PC}	$m_{\text{AQD I}}$	$m_{\text{AED I}}$	$m_{\text{ALD I}}$	$m_{\text{AQD II}}$	$m_{\text{AED II}}$	$m_{\text{ALD II}}$
8	4.99	5.01	4.97	4.98	5.03	4.97
10	5.42	5.48	5.37	5.40	5.52	5.38
12	5.82	5.90	5.74	5.79	5.96	5.75
14	6.19	6.30	6.07	6.15	6.37	6.09
16	6.53	6.67	6.39	6.49	6.76	6.41
18	6.86	7.02	6.68	6.81	7.13	6.71

TABLE X: Mass spectra (GeV) of pomerons as a function of J^{PC} , taking into account exclusively lattice QCD data up to $J^{PC} = 6$. The second and fifth columns display the CE of the anomalous quadratic dilaton I and II (AQD I and II) models; the third and sixth columns show the pomerons CE computed from the anomalous exponential dilaton I and (AED I and II) models; the fourth and seventh columns show the CE, respectively computed from the anomalous linear dilaton I and II (ALD I and II) models.

One can compare the pomeron mass spectra in Tables VIII and X, computed from the CE Regge trajectories, with the ones purely computed from AdS/QCD in Tables XI and XII.

Pomeron mass spectra: anomalous linear dilaton I model

J^{PC}	$k = 0.17$ $\gamma_0 = -1.0$	$k = 0.16$ $\gamma_0 = -1.5$	$k = 0.13$ $\gamma_0 = -1.0$	$k = 0.255$ $\gamma_0 = -1.995$
8	5.073	4.813	4.494	5.837
10	6.177	5.882	5.464	7.176
12	7.281	6.952	6.435	8.519
14	8.385	8.023	7.405	9.863
16	9.489	9.095	8.376	11.209
18	10.594	10.167	9.347	12.555

TABLE XI: Pomerons mass spectra (GeV) as a function of J^{PC} , for the anomalous linear dilaton I model, from AdS/QCD, for several values of k and γ_0 .

The fourth column in Table X, for the values $k = 0.255$ and $\gamma_0 = -1.995$, represents the pomeron mass spectra obtained purely from AdS/QCD. These values were used to derive the CE Regge trajectories (45, 59) — for the hybrid model considering exclusively lattice QCD data, up to $J^{PC} = 6$, and including for $J^{PC} = 8, 10$ the pomeron mass spectra (30) and extrapolating for $J^{PC} = 12, \dots, 18$ the mass spectra — and (81, 99) — regarding exclusively lattice QCD data, up to $J^{PC} = 6$, and extrapolating for $J^{PC} = 8, \dots, 18$ the mass spectra. Thence, the values $k = 0.255$ and $\gamma_0 = -1.995$ have been employed to compute the CE with the respect to both J^{PC} and the pomeron mass spectrum, represented by cyan [orange] points for the anomalous linear dilaton I [II], respectively in Figs. 8 and 9. Therefore, for effects of direct comparison, the fifth column in Table XI plays an important role, when one looks at the corresponding pomeron mass spectra in Tables VIII and X, obtained by the analysis of the CE Regge trajectories. In fact, let us compare the pomeron mass spectra, generated from the anomalous linear dilaton I model in the hybrid model in Table VIII, to the pomeron mass spectra obtained purely from AdS/QCD in Table XI. Let us denote by Δ_k the difference between the respectively derived masses when $J^{PC} = k$. Therefore, when $J^{PC} = 12$, $\Delta_{12} = 16.5\%$, whereas the value $J^{PC} = 14$ yields $\Delta_{12} = 14.6\%$. Also, $\Delta_{16} = 24.3\%$ for $J^{PC} = 16$ and $\Delta_{18} = 34.7\%$. The increment of the mass difference, as k increases, is understood as the uncertainty in the models for higher spin pomeron resonances. A similar reasoning can be obtained for all other dilaton models.

Pomeron mass spectra: anomalous linear II model

J^{PC}	$k = 0.2$ $\gamma_0 = -1.5$	$k = 0.2$ $\gamma_0 = 1.595$	$k = 0.12$ $\gamma_0 = 1.233$
8	5.626	5.841	4.605
10	6.838	7.032	5.538
12	8.046	8.223	6.471
14	9.252	9.415	7.404
16	10.457	10.607	8.337
18	11.660	11.800	9.271

TABLE XII: Pomerons mass spectra (GeV) as a function of J^{PC} , for the anomalous linear dilaton II model, from AdS/QCD.

IV. CONCLUDING REMARKS

The CE was computed for pomerons, for six dilaton models, namely, the anomalous quadratic dilaton I and II, the anomalous linear dilaton I and II, and the anomalous exponential dilaton I and II models. Two types of configurational-entropic Regge trajectories were derived, for the pomeron family resonances. The first CE Regge trajectory relates the CE of the pomerons to their J^{PC} spin, represented by Eqs. (43 – 48), respectively for the anomalous quadratic I, the anomalous exponential dilaton I, the anomalous linear I, the anomalous quadratic II, the anomalous exponential II, and the anomalous linear II dilaton models. These CE Regge trajectories are interpolation curves, taking into account exclusively lattice QCD data, up to $J^{PC} = 6$, and including for $J^{PC} = 8, 10$ the pomeron mass spectra (30), shown in Fig. 8. Higher J^{PC} pomeron resonances have their CE extrapolated from those CE Regge trajectories. The second type of CE Regge trajectories relates the CE of pomerons with their mass spectra, for the six dilaton models, represented by Eqs. (49, 54, 59, 64, 69, 74), respectively shown in the plots of Fig. 9. Consequently, the pomeron family mass spectra were extrapolated from the CE Regge trajectories. A range for the mass spectra of pomerons with higher J^{PC} was then estimated with good accuracy. Higher spin pomeron resonances, beyond $J^{PC} = 18$, are not explored, since they are configurationally very unstable, with huge values of CE. Even states with $J^{PC} > 12$ are unlikely to be experimentally detected, at least with proposed experiments that have been run in LHC.

For both the protocols adopted, a) in Subsect. III A computing the CE of pomerons as a function of J^{PC} , taking into account lattice QCD data up to $J^{PC} = 6$, and including for $J^{PC} = 8, 10$ the pomeron mass spectra (30); and b) in Subsect. III B, taking into account exclusively lattice QCD data, up to $J^{PC} = 6$ — both Figs. 8 and 10 exhibit the pomeron resonances in the anomalous exponential dilaton I as more unstable, from the configurational point of view, when compared with the other

dilaton models approached. Besides, the linear dilaton model II encompasses more stable pomeron resonances. More configurationally stable resonances represent quantum states that are more dominant and prevalent, from the phenomenological standpoint [10, 11, 15]. Hence, this method points to pomeron resonances that may be more detectable and observable in experiments.

From the experimental point of view, the $f_2(1950)$ resonance, with $J^{PC} = 2^{++}$ and mass 1.944 ± 0.012 GeV [9], has been recently proposed to be a promising candidate for the pomeron ground state [66]. Since there is no experimental data available in PDG for high J^{PC} resonances pomerons, then at least the obtained mass spectra should be compared to lattice QCD data. However, available calculations encompass just low J^{PC} pomeron resonances. Hence, the analysis and tables heretofore obtained in this work, containing the pomeron mass spectra for the six dilaton models, allows us to create a quite useful phenomenological database. In particular, these results complete a data bank for high-energy reactions and decays, having the pomeron as a byproduct in high-energy experiments. The obtained pomeron mass spectra, in several backgrounds here studied, may be directly employed for testing and developing aspects of AdS/QCD models. Moreover, the CE Regge trajectories implement a new method of deriving the mass spectra of the pomeron family, in the anomalous linear I and II, the anomalous exponential I and II, and the anomalous

quadratic dilatonic I and II backgrounds as well. These CE Regge trajectories provide the derivation of the mass spectra of higher J^{PC} pomeron resonances, acting as a benchmarking of AdS/QCD models.

Furthermore, it would be interesting to extend the analysis made in this paper considering different profiles for the dilaton field, and also considering glueball operators of twist-2, since there are some works which propose and consider the pomeron to be associated with a twist-2 object [51, 63, 67]. Here, we considered the twist-4 approach, since we were also interested in including the scalar glueball sector. However, there are some shreds of evidence, within the holographic approach, which show that the mass of the scalar and tensor glueballs are degenerate. Here, we provided one more evidence for this in the case of the exponential dilaton profile. Finally, another possibility is to extend the analysis we have made here to the odd-spin glueballs, which are associated with the odderon.

Acknowledgments: DMR is supported by the National Council for Scientific and Technological Development – CNPq (Brazil) under Grant No. 152447/2019-9. RdR is grateful to FAPESP (Grant No. 2017/18897-8 and No. 2015/10270-0) and to the National Council for Scientific and Technological Development – CNPq (Grants No. 303390/2019-0, No. 406134/2018-9 and No. 303293/2015-2), for partial financial support.

-
- [1] C. E. Shannon, Bell Syst. Tech. J. **27** (1948) 379.
[2] M. Gleiser and N. Stamatopoulos, Phys. Lett. B **713** (2012) 304 [arXiv:1111.5597 [hep-th]].
[3] M. Gleiser and N. Stamatopoulos, Phys. Rev. D **86** (2012) 045004 [arXiv:1205.3061 [hep-th]].
[4] M. Gleiser and D. Sowinski, Phys. Lett. B **747** (2015) 125 [arXiv:1501.06800 [cond-mat.stat-mech]].
[5] G. Karapetyan, EPL **117** (2017) 18001 [arXiv:1612.09564 [hep-ph]].
[6] G. Karapetyan, EPL **118** (2017) 38001 [arXiv:1705.10617 [hep-ph]].
[7] G. Karapetyan, Phys. Lett. B **781** (2018) 201 [arXiv:1802.09105 [nucl-th]].
[8] G. Karapetyan, Phys. Lett. B **786** (2018) 418 [arXiv:1807.04540 [nucl-th]].
[9] M. Tanabashi *et al.* [ParticleDataGroup], Phys. Rev. D **98** (2018) 030001.
[10] A. E. Bernardini and R. da Rocha, Phys. Lett. B **762** (2016) 107 [arXiv:1605.00294 [hep-th]].
[11] A. E. Bernardini and R. da Rocha, Phys. Rev. D **98** (2018) 126011 [arXiv:1809.10055 [hep-th]].
[12] L. F. Ferreira and R. da Rocha, Phys. Rev. D **99** (2019) no.8, 086001 [arXiv:1902.04534 [hep-th]].
[13] N. Barbosa-Cendejas, R. Cartas-Fuentevilla, A. Herrera-Aguilar, R. R. Mora-Luna and R. da Rocha, Phys. Lett. B **782** (2018) 607 [arXiv:1805.04485 [hep-th]].
[14] L. F. Ferreira and R. da Rocha, Phys. Rev. D **101** (2020) 106002 [arXiv:1907.11809 [hep-th]].
[15] A. E. Bernardini, N. R. F. Braga and R. da Rocha, Phys. Lett. B **765** (2017) 81 [arXiv:1609.01258 [hep-th]].
[16] N. R. F. Braga and R. da Rocha, Phys. Lett. B **776** (2018) 78 [arXiv:1710.07383 [hep-th]].
[17] N. R. F. Braga, L. F. Ferreira and R. da Rocha, Phys. Lett. B **787** (2018) 16 [arXiv:1808.10499 [hep-ph]].
[18] N. R. Braga and R. da Mata, Phys. Rev. D **101** (2020) 105016 [arXiv:2002.09413 [hep-th]].
[19] G. Karapetyan, EPL **129** (2020) no.1, 18002 [arXiv:1912.10071 [hep-ph]].
[20] A. Goncalves da Silva and R. da Rocha, Phys. Lett. B **774**, 98 (2017) [arXiv:1706.01482 [hep-th]].
[21] C. W. Ma and Y. G. Ma, Prog. Part. Nucl. Phys. **99** (2018) 120 [arXiv:1801.02192 [nucl-th]].
[22] P. Colangelo and F. Lopalco, Phys. Lett. B **788** (2019) 500 [arXiv:1811.05272 [hep-ph]].
[23] L. F. Ferreira and R. da Rocha, Phys. Rev. D **101** (2020) 106002 [arXiv:2004.04551 [hep-th]].
[24] R. Casadio and R. da Rocha, Phys. Lett. B **763** (2016) 434 [arXiv:1610.01572 [hep-th]].
[25] M. Gleiser and N. Jiang, Phys. Rev. D **92** (2015) 044046 [arXiv:1506.05722 [gr-qc]].
[26] N. R. F. Braga and R. da Rocha, Phys. Lett. B **767** (2017) 386 [arXiv:1612.03289 [hep-th]].
[27] N. R. Braga, Phys. Lett. B **797** (2019) 134919 [arXiv:1907.05756 [hep-th]].
[28] C. O. Lee, Phys. Lett. B **790** (2019) 197 [arXiv:1812.00343 [gr-qc]].
[29] C. O. Lee, Phys. Lett. B **772** (2017) 471 [arXiv:1705.09047 [gr-qc]].

- [30] M. Gleiser, M. Stephens and D. Sowiński, *Phys. Rev. D* **97** (2018) 096007 [arXiv:1803.08550 [hep-th]].
- [31] R. A. C. Correa, D. M. Dantas, C. A. S. Almeida and R. da Rocha, *Phys. Lett. B* **755** (2016) 358 [arXiv:1601.00076 [hep-th]].
- [32] W. T. Cruz, D. M. Dantas, R. V. Maluf and C. A. S. Almeida, *Annalen Phys.* **531** (2019) 1970035
- [33] C. O. Lee, *Phys. Lett. B* **800** (2020) 135030 [arXiv:1908.06074 [hep-th]].
- [34] D. Bazeia, D. C. Moreira and E. I. B. Rodrigues, *J. Magn. Magn. Mater.* **475** (2019) 734.
- [35] A. Alves, A. G. Dias, R. da Silva, *Physica* **420** (2015) 1 [arXiv:1408.0827 [hep-ph]].
- [36] A. Alves, A. G. Dias, R. da Silva, *Braz. J. Phys.* **47** (2017) 426.
- [37] E. Witten, *Riv. Nuovo Cim.* **43** (2020) 3 [arXiv:1805.11965 [hep-th]].
- [38] J. Erlich, E. Katz, D. T. Son and M. A. Stephanov, *Phys. Rev. Lett.* **95** (2005) 261602 [arXiv:hep-ph/0501128].
- [39] A. Karch, E. Katz, D. T. Son and M. A. Stephanov, *Phys. Rev. D* **74** (2006) 015005 [hep-ph/0602229].
- [40] S. J. Brodsky, G. F. de Teramond, H. G. Dosch, J. Erlich, *Phys. Rept.* **584** (2015) 1 [arXiv:1407.8131 [hep-ph]].
- [41] J. M. Maldacena, *Int. J. Theor. Phys.* **38** (1999) 1113 [Adv. Theor. Math. Phys. **2** (1998) 231 [hep-th/9711200]].
- [42] E. Witten, *Adv. Theor. Math. Phys.* **2** (1998) 253 [hep-th/9802150].
- [43] S. S. Gubser, I. R. Klebanov and A. M. Polyakov, *Phys. Lett. B* **428** (1998) 105 [arXiv:hep-th/9802109].
- [44] J. Polchinski and M. J. Strassler, *Phys. Rev. Lett.* **88** (2002) 031601 [hep-th/0109174].
- [45] H. Boschi-Filho and N. R. F. Braga, *Eur. Phys. J. C* **32** (2004) 529 [hep-th/0209080].
- [46] H. Boschi-Filho and N. R. F. Braga, *JHEP* **0305** (2003) 009 [hep-th/0212207].
- [47] T. Gutsche, S. Kuleshov, V. E. Lyubovitskij and I. T. Obukhovskiy, *Phys. Rev. D* **94**, no.3, 034010 (2016) [arXiv:1605.01035 [hep-ph]].
- [48] M. Sergeenko, *EPL* **89** (2010) 11001 [arXiv:1107.1671 [hep-ph]].
- [49] H. B. Meyer and M. J. Teper, *Phys. Lett. B* **605** (2005) 344 [arXiv:hep-ph/0409183 [hep-ph]].
- [50] J. F. Donoghue, K. Johnson and B. A. Li, *Phys. Lett. B* **99** (1981) 416.
- [51] C. Ewerz, M. Maniatis and O. Nachtmann, *Annals Phys.* **342**, 31-77 (2014) [arXiv:1309.3478 [hep-ph]].
- [52] D. Li and M. Huang, “Dynamical holographic QCD model for glueball and light meson spectra,” *JHEP* **1311**, 088 (2013) [arXiv:1303.6929 [hep-ph]].
- [53] D. M. Rodrigues, E. Folco Capossoli and H. Boschi-Filho, *EPL* **122** (2018) no.2, 21001 [arXiv:1611.09817 [hep-ph]].
- [54] A. Ballon-Bayona, H. Boschi-Filho, L. A. H. Mamani, A. S. Miranda and V. T. Zanchin, *Phys. Rev. D* **97** (2018) no. 4, 046001 [arXiv:1708.08968 [hep-th]].
- [55] W. de Paula, T. Frederico, H. Forkel and M. Beyer, *Phys. Rev. D* **79**, 075019 (2009) [arXiv:0806.3830 [hep-ph]].
- [56] U. Gursoy and E. Kiritsis, *JHEP* **0802** (2008) 032 [arXiv:0707.1324 [hep-th]].
- [57] U. Gursoy, E. Kiritsis and F. Nitti, *JHEP* **0802** (2008) 019 [arXiv:0707.1349 [hep-th]].
- [58] U. Gursoy, E. Kiritsis, L. Mazzanti and F. Nitti, *JHEP* **05**, 033 (2009) [arXiv:0812.0792 [hep-th]].
- [59] Z. Fang, Y. L. Wu and L. Zhang, *Phys. Rev. D* **100**, no.5, 054008 (2019) [arXiv:1904.04695 [hep-ph]].
- [60] A. Ballon-Bayona, R. Carcasss Quevedo, M. S. Costa and M. Djuri, *Phys. Rev. D* **93**, 035005 (2016) [arXiv:1508.00008 [hep-ph]].
- [61] E. Folco Capossoli, D. Li and H. Boschi-Filho, *Eur. Phys. J. C* **76**, no. 6, 320 (2016) [arXiv:1604.01647 [hep-ph]].
- [62] E. Folco Capossoli, D. Li and H. Boschi-Filho, *Phys. Lett. B* **760**, 101 (2016) [arXiv:1601.05114 [hep-ph]].
- [63] I. Szanyi, L. Jenkovszky, R. Schicker and V. Svinotzelskyi, *Nucl. Phys. A* **998**, 121728 (2020) [arXiv:1910.02494 [hep-ph]].
- [64] N. R. Constable and R. C. Myers, *JHEP* **9910**, 037 (1999) [hep-th/9908175].
- [65] D. M. Rodrigues, E. Folco Capossoli and H. Boschi-Filho, *Phys. Rev. D* **95**, no. 7, 076011 (2017) [arXiv:1611.03820 [hep-th]].
- [66] A. Godizov, *Eur. Phys. J. C* **76** (2016) no.7, 361 [arXiv:1604.01689 [hep-ph]].
- [67] I. Iatrakis, A. Ramamurti and E. Shuryak, *Phys. Rev. D* **94**, no.4, 045005 (2016) [arXiv:1602.05014 [hep-ph]].